communications physics

A Nature Portfolio journal

Article

https://doi.org/10.1038/s42005-025-02114-0

Förster valley-orbit coupling and topological lattice of hybrid moiré excitons

Huiyuan Zheng [1,2], Ci Li [3], Hongyi Yu [4] & Wang Yao [1,2]

Hybrid excitons in moiré superlattices of two-dimensional (2D) semiconductors inherit the electric dipole, strong moiré trapping, and stacking optical selection rules from its interlayer part, whereas the intralayer part is intended for enhancing optical coupling strength. Here, we show that electron-hole Coulomb exchange, or Förster type multipole-multipole coupling, in the intralayer component qualitatively alters the properties of moiré excitons, enabling their coherent hopping between moiré traps laterally separated over 10 nm and/or across layers, where their kinetic propagation is completely suppressed. Valley-flip hopping channels are found as significant as the valley-conserving ones, leading to rich possibilities to tailor valley-orbit-couplings and introduce non-trivial topology to the moiré exciton superlattice. In twisted $MoTe_2$ where hybrid moiré excitons feature a symmetry protection from radiative recombination, we show that Förster valley-orbit-coupling can give rise to a rich topological phase diagram.

In bilayer 2D semiconductors, the moiré pattern introduced by twist and/or lattice mismatch can endow excitons with a plethora of intriguing opportunities, from applications in optoelectronics to the exploration of quantum matters of fundamental interest[1–9]. In heterobilayers, the lowest energy excitons have an interlayer configuration carrying a permanent electric dipole, which underlies electric field tunability of exciton energy and pronounced exciton–exciton interaction[10]. In the moiré-defined periodic landscape[11], these interlayer excitons are tightly confined in an ordered array of moiré traps, exhibiting behavior akin to quantum-dot-like single-photon emitters[3,5,12,13]. Such quantum emitters uniquely feature optical selection rules conditioned on the spin and valley indices as well as local atomic registries[3,14,15], implying rich optoelectronic control possibilities. While the layer separation of electron and hole components has led to a weak coupling to light, the resultant long radiative lifetime is on the other hand favorable for the exploration of exciton many-body physics in Bose-Hubbard lattices with the strong dipolar interaction[16–18].

When light-coupling is favored, the interlayer moiré excitons can be brightened through hybridization with a nearly resonant intralayer exciton. In heterobilayers, this is made possible under various compound choices that have nearly aligned conduction or valence bands[8,19–21] (Fig. 1a). In moiré traps of different local stacking registries, the C_3 rotational symmetry dictates different center-of-mass envelope forms of the intralayer component hybridized to a tightly trapped interlayer exciton wavepacket (Fig. 1c), whereas an *s*-wave envelope leads to brightening. The intralayer wavefunction overlap between electron and hole also underlies pronounced electron–hole Coulomb exchange that can non-locally transfer exciton either in momentum space (i.e. between valleys[22–24]), or in real space[25–28]. This is essentially the Förster non-radiative dipole-dipole coupling underlying the fluorescence resonance energy transfer[29].

Hybrid moiré excitons are also hosted by homobilayers of near 0° twisting, such as twisted $MoTe_2$ (t-$MoTe_2$) that has caught great attention for the fractional quantum anomalous Hall effects[30–33]. Because of the stacking-dependent interfacial electrical polarization[34,35], interlayer excitons are trapped at the MX and XM stacking regions with opposite layer configuration (electric dipole), where trapping energy can largely compensate the binding energy difference from an intralayer exciton, leading to their hybridization[36]. The C_3 rotational symmetry, however, dictates that the hybridized intralayer component has a *p*-wave envelope that leads to vanishing optical transition dipole, therefore protected from radiative recombination. Such homobilayers offer a platform to explore dipolar ordering of long-lived hybrid moiré excitons, where spontaneous C_3 symmetry breaking manifests a unique optical signature[36].

Here, we show that the moiré exciton is qualitatively altered by its intralayer component, in which sizable Förster-type multipole–multipole coupling enables the hybrid exciton to hop coherently and non-locally between moiré traps across layers and/or over 10 nm apart laterally, where kinetic propagation is completely suppressed. Valley-flip hopping channels are found as significant as the valley-conserving ones, and we identify their non-monotonic dependence on hopping distance, with phase pattern dependent on valley indices and envelope forms of the intralayer

[1]New Cornerstone Science Laboratory, Department of Physics, University of Hong Kong, Hong Kong, China. [2]HK Institute of Quantum Science & Technology, University of Hong Kong, Hong Kong, China. [3]School of Physics and Electronics, Hunan University, Changsha, 410082, China. [4]School of Physics and Astronomy, Sun Yat-sen University (Zhuhai Campus), Zhuhai, 519082, China. e-mail: wangyao@hku.hk

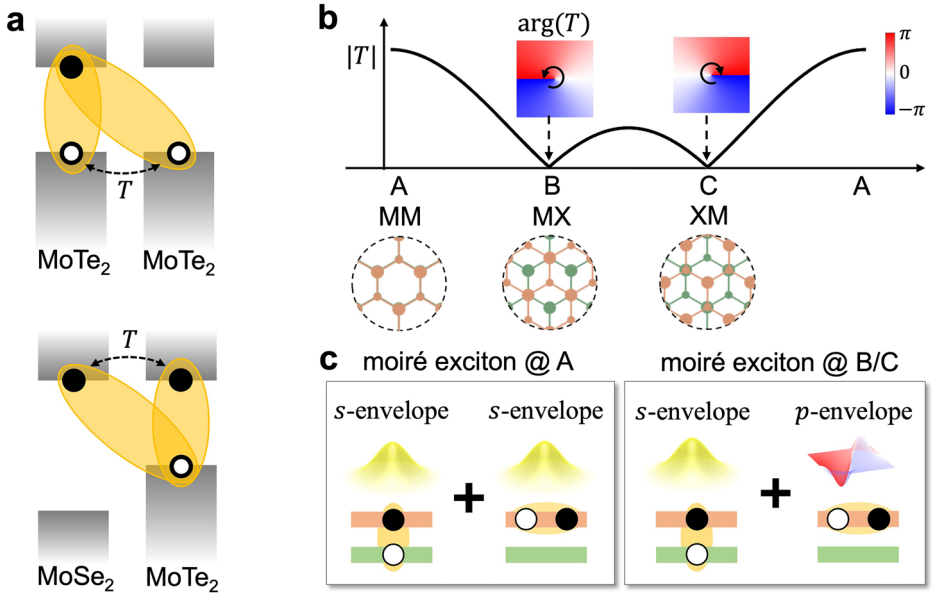

Fig. 1 | Exciton hybridization in TMD moiré structures. a Schematics of hybrid excitons in TMD homobilayers (upper) and heterobilayers (lower). Black (white) dots denote the electron (hole). T denotes interlayer hopping. **b** Spatially varying interlayer hopping in R-stacking bilayers. Hopping vanishes at the high symmetry points B (MX) and C (XM), and has a p-wave form in their vicinity. The insets below show their local stacking. The phase of T is color-coded to show the counterclockwise and clockwise winding patterns around the B and C points, respectively. In the vicinity of A point of MM stacking, the hopping has an s-wave form. **c** Schematics of the center-of-mass envelope functions of the hybrid exciton at high symmetry points. The minor intralayer component exhibits an s-wave and a p-wave envelope at A point and B/C points, respectively, whereas the major interlayer component always has an s-wave envelope for the lowest energy state in the confinement. Black (white) dots represent the electron (hole), indicating their intralayer/interlayer components.

Table 1 | Symmetry-dictated properties of hybrid moiré excitons trapped at high symmetry points in R- and H-stacking bilayers

	R-stacking						H-stacking					
Electric dipole	**z**			**−z**			**z**			**−z**		
High symmetry point	MM	MX	**XM**	MM	**MX**	XM	MM	MX	XX	MM	MX	XX
Optical selection rule	σ_+	↕	$\boldsymbol{\sigma_-}$	σ_+	$\boldsymbol{\sigma_-}$	↕	σ_+	σ_-	↕	σ_+	σ_-	↕
Intralayer envelope	s	p_-	$\boldsymbol{p_+}$	s	$\boldsymbol{p_+}$	p_-	s	p_+	p_-	s	p_+	p_-

The quantities listed are the direction of electric dipole; optical selection rule of interlayer exciton (σ_+, σ_- circularly and out-of-plane (↕) linearly polarized light); and envelope form of the minor intralayer component. The hybrid moiré exciton considered is the lowest energy configuration involving only A excitons, and for H-stacking, this means the hybridization is through the electron hopping only. The major interlayer component is assumed an s-wave form, and only the spin-singlet exciton with spin-down hole is shown. The bold values correspond to moiré excitons in R-homobilayer.

component. This leads to rich possibilities to tailor valley–orbit-coupling (VOC) forms, which can introduce non-trivial topology to the moiré exciton superlattice. We demonstrate this possibility for the long-lived excitons in twisted $MoTe_2$ bilayers, where Förster-type quadrupole–quadrupole couplings link the two otherwise isolated exciton sublattices of opposite layer configurations and give rise to a rich topological phase diagram.

Results

Layer hybridization of moiré-trapped excitons

In a long-wavelength moiré pattern, the C_3 rotational symmetry dictates that the potential energy minima and maxima of the exciton must correspond to the three high symmetry points in a supercell where local stacking registries are C_3 invariant. We focus on moiré excitons trapped at these points with a major interlayer component of an s-wave envelope, and a minor intralayer component (throughout this paper, 'envelope function' refers specifically to the exciton's center-of-mass wave function). Their hybridization is determined by the interlayer tunneling matrix element T between conduction or valence band edges. At the $\pm K$ valleys, the large crystal momentum leads to a stacking selection rule that dictates T must vanish at two out of the three high symmetry stacking points[37]. In the first harmonic approximation[38], T as a function of space coordinate $\mathbf{R}$ takes the form of $\sum_j \exp(iC_3^j \delta\mathbf{K}\cdot\mathbf{R})$[37,39], $\delta\mathbf{K}$ being the valley mismatch between layers. The example for the R-type bilayer is shown in Fig. 1b. In the vicinity of B (MX stacking) and C (XM) points, interlayer tunneling takes the p-wave forms $T \propto \delta R_x + i\delta R_y$ and $\delta R_x - i\delta R_y$, respectively, where $\delta\mathbf{R}$ denotes the displacement from the high symmetry points. In the vicinity of the A (MM) point, T is approximately a constant. Lattice reconstructions can quantitatively change the function $T(\mathbf{R})$, but not these symmetry-dictated leading order forms near the three high symmetry points. These determine the envelope function of the minor intralayer component. For instance, hybrid moiré exciton has an intralayer component in p-wave envelope at B and C points in R-type bilayer (Fig. 1c).

Table 1 summarizes the symmetry-dictated envelope forms of intralayer component in moiré hybrid excitons at the high symmetry points in R- (near 0°) and H-type (near 60°) bilayers, which can also be deduced from optical selection rules (see Supplementary Note 1). In a hybrid moiré exciton, the allowed intralayer component must have an optical dipole with the same polarization as the interlayer component. However, the latter has a valley optical selection rule that also depends on the stacking registries (c.f. Table 1)[3]. At high symmetry points where the intra- and inter-layer valley selection rules differ, a p-type envelope is necessitated to reshape the optical dipole polarization of the intralayer component. Such hybrid excitons have a tiny optical dipole and long radiative lifetime (see Supplementary Note 2), just like their interlayer component. Nevertheless, having an intralayer component can activate Förster coupling, which enables a coherent nonlocal hopping.

Förster type multipole-multipole coupling of intralayer exciton wavepackets

Electron-hole Coulomb exchange can annihilate an intralayer exciton at valley τ of layer n and create another at τ' valley of layer n' (Fig. 2a). In the basis of exciton momentum eigenstates $|\tau, n, \mathbf{q}\rangle$, such a Förster coupling takes the form: $\hat{J}^{n',n}_{\tau',\tau}(\mathbf{q}) = (-1)^{\frac{\tau'-\tau}{2}} e^{-i(\tau'\theta_{n'}-\tau\theta_n)} e^{-i(\tau'-\tau)\varphi_q} J e^{-qz}\frac{q}{K}$[25,28], where $\tau, \tau' = \pm 1$, $\mathbf{q}$ is the exciton center-of-mass momentum with φ_q being the

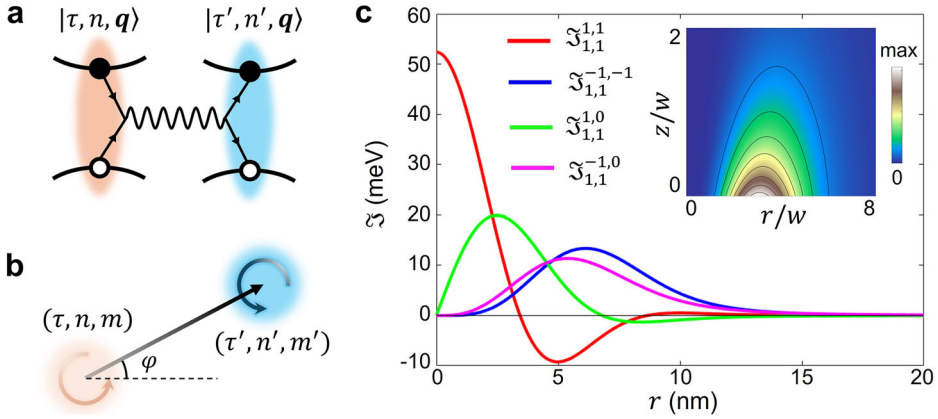

Fig. 2 | Förster coupling of moiré exciton wavepackets. a Schematic of Coulomb exchange that annihilates an electron–hole pair in valley τ at layer n and creates one in valley τ' of layer n'. **b** The process in **a** effectively realizes non-local hopping—Förster coupling—of moiré exciton wavepackets, which is further determined by the envelope form (azimuthal quantum number m, wavepacket width w) of the intralayer component. **c** Förster coupling strength of various channels $\mathfrak{J}^{\tau',m'}_{\tau,m}$, as function of in-plane distance (r) evaluated at out-of-plane distance $z = 0$. The subscripts (superscripts) denote the valley index τ (τ') and azimuthal index m (m') of the initial (final) states. The inset shows the $\mathfrak{J}^{-1,-1}_{1,1}$ channel as function of the dimensionless in-plane and out-of-plane distances r/w, z/w. Wavepacket width $w = 2$ nm is used in calculation.

azimuthal angle, z is the distance between layer n and n', and θ_n denotes the twisting angle of layer n. Now we consider this coupling between localized exciton wavepacket states of C_3 rotational symmetry (Fig. 2b), which are further classified by the azimuthal quantum number m: $|\psi_{\tau,n,m}(\mathbf{r}_c)\rangle = \sum_{\mathbf{q}} e^{-i\mathbf{q}\cdot\mathbf{r}_c} f_m(q) e^{im\varphi_q} |\tau, n, \mathbf{q}\rangle$, $m = 0$ or ± 1, corresponding to s- or p-wave envelope. $\mathbf{r}_c$ denotes the wavepacket center, and $f_m(q)$ is a real function accounting for the radial dependence. Förster coupling between a pair of exciton wavepacket states of in-plane displacement $\mathbf{r} = (r, \varphi_r) = \mathbf{r}'_c - \mathbf{r}_c$ is of the form (see Supplementary Note 3 for derivation details):

$$J^{\tau',n',m'}_{\tau,n,m}(\mathbf{r}) = \left\langle \psi_{\tau',n',m'}(\mathbf{r}'_c) | \hat{J} | \psi_{\tau,n,m}(\mathbf{r}_c) \right\rangle = e^{-i(m'-m)\frac{\pi}{2}} e^{-i(\tau'\theta_{n'} - \tau\theta_n)} e^{-i(\tau'-\tau+m'-m)\varphi_r} \mathfrak{J}^{\tau',m'}_{\tau,m}(r, z, w) \quad (1)$$

The angular part is in the form of a phase factor, where $(\tau' - \tau + m' - m)$ are integers between ± 4. The radial part $\mathfrak{J}^{\tau',m'}_{\tau,m}(r)$ is a real function, with dependence on the layer distance z and wavepacket width w. For calculations hereafter, we adopt the wavepacket envelopes to be eigenfunctions of 2D harmonic traps[26]: $f_m(q) \propto w^{|m|+1} q^{|m|} e^{-w^2 q^2/2}$. Figure 2c plots the radial dependence of several representative intra- and inter-valley Förster coupling channels. Notably, compared to the intravalley ones, the intervalley channels peak at a larger hopping distance r ~5–10 nm, where the overlap between the initial and final state wavepackets is already negligible. We also identify scaling behaviors (see Supplementary Note 3): (1) $w\mathfrak{J}^{\tau',m'}_{\tau,m}$ is a function of the dimensionless distances r/w and z/w only; (2) for $r > 10w$, $\mathfrak{J}^{\tau',m'}_{\tau,m}$ is asymptotic to $r^{-(3+|m|+|m'|)}$, suggesting that p-envelope excitons are coupled via a quadrupole moment[40]. For hybrid excitons, their Förster coupling can be obtained by multiplying a factor $\eta \equiv \psi_i \psi_f^*$, where ψ_i (ψ_f) is the normalized probability amplitude of intralayer component in the initial (final) state.

Förster valley-orbit coupling in t-MoTe$_2$

In the following, we focus on R-stacking t-MoTe$_2$, where moiré excitons are trapped at the B (MX) and C (XM) points with opposite layer configurations (Fig. 3a), such that kinetic propagation has no nearest-neighbor terms, leaving the two sublattices uncoupled. Pronounced hybrdization of a p-wave intralayer component is expected[36], where our analysis finds an azimuthal index locked to the valley $m = \tau$ (see Table 1). Through such intralayer component, Förster coupling not only links the two sublattices, but also introduces a pronounced VOC. The relevant intra- and inter-valley channels are $\mathfrak{J}^{1,1}_{1,1}$ and $\mathfrak{J}^{-1,-1}_{1,1}$, the latter having a phase factor dependent on hopping direction $e^{4i\varphi}$ (Fig. 3b, c.f. Eq. (1)). The Förster VOC in the honeycomb superlattice can be written as (details in Supplementary Note 5):

$$H^{voc}_{i'i} = b^\dagger_{i'} \left[\alpha_{i'i} - \beta_{i'i} \left(\tau_x \cos 4\varphi_{i'i} + \tau_y \sin 4\varphi_{i'i} \right) \right] b_i, \quad (2)$$

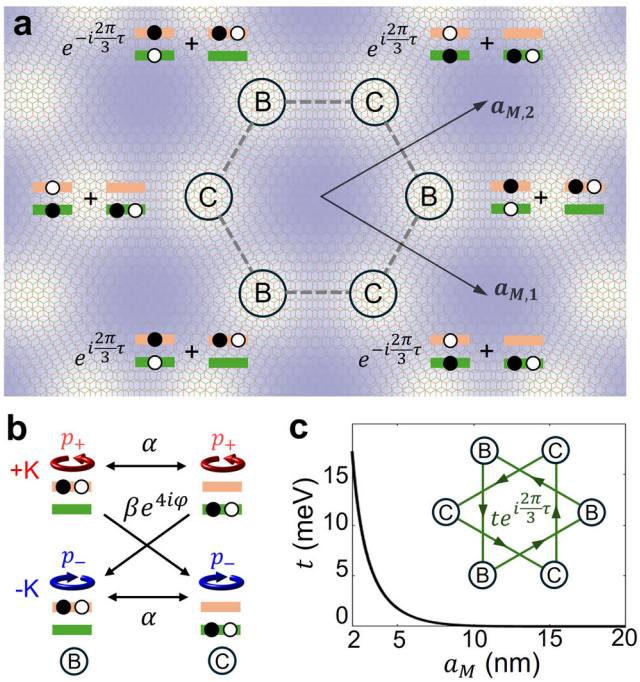

Fig. 3 | Hybrid moiré exciton lattice in the twisted MoTe$_2$ homobilayer. a Schematics of hybrid moiré excitons trapped at the B and C sites in t-MoTe$_2$. Black (white) dots denote the electron (hole), and they are distributed in top (orange) and bottom (green) layer. The symbols of inter- and intra-layer configurations correspond to wavepackets of the form $|\psi^{\text{inter/intra}}_{\tau,m}(\mathbf{r}_c)\rangle = \sum_{\mathbf{q}} e^{-i\mathbf{q}\cdot\mathbf{r}_c} f(q) e^{im\varphi_q} |X^{\text{inter/intra}}_{\tau,\mathbf{q}}\rangle$, $\mathbf{r}_c$ denoting wavepacket center, and this gauge choice leads to the $\mathbf{r}_c$-dependent phase factor in the linear superposition (see Supplementary Note 2). **b** Nearest-neighbor intravalley and intervalley Förster coupling between moiré exciton states at B and C site, which have p_+ (p_-) intralayer envelope at $K(-K)$ valley. **c** Kinetic propagation amplitude as a function of moiré period. The inset shows the kinetic propagation as a next-nearest-neighbor complex hopping, $\tau = \pm 1$ is the valley index.

where $b_i \equiv (b_{i,K}, b_{i,-K})^T$ is the exciton annihilation operator at site i, $\tau_{x,y,z}$ are the Pauli matrices for the valley pseudospin, and $\varphi_{i'i}$ denotes the hopping angle from site i to i'. $\alpha_{i'i} = \eta\mathfrak{J}^{1,1}_{1,1}$ and $\beta_{i'i} = \eta\mathfrak{J}^{-1,-1}_{1,1}$, and $\mathfrak{J}$ are evaluated at the corresponding hopping distance, whose non-monotonic dependence can be used to tailor the relative strengths of α and β through tuning the twisting angle. η is the weight of the intralayer component in the alike initial and final states, and it depends on several key energy scales (c.f. ref. 36): (i) the amplitude of interlayer carrier hopping; (ii) the depth of moiré trapping potential; (iii) the binding energy difference between inter- and intra-layer excitons. The last quantity can be tunable through the dielectric

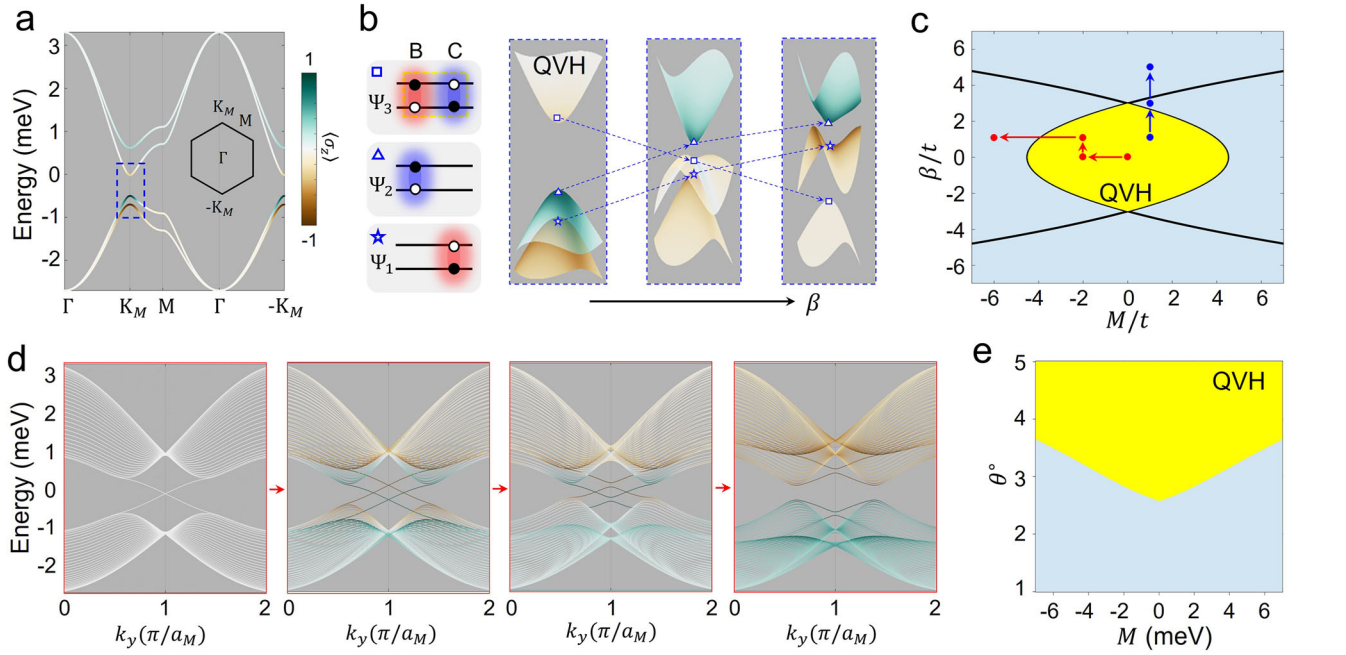

Fig. 4 | Dispersion and phase diagram of hybrid moiré exciton lattice. a An exemplary dispersion of hybrid moiré exciton in t-$MoTe_2$, color coded with the sublattice polarization $\langle\sigma_z\rangle$. $t = 0.1$ meV, $\alpha = 1$ meV, $\beta = M = 0.1$ meV. **b** Left: layer and valley configurations of three states at the mini-Brillouin zone corner K_M enclosed by the dashed box in **a**. Red (blue) denote K ($-K$) valley excitons. Right: inversions between the three states, upon the increase of intervalley Förster coupling β. **c** Topological phase diagram as function of β and interlayer bias M. $t = 0.1$ meV and $\alpha = 1$ meV. The two parabolas mark the points of inversion of Ψ_3 with Ψ_1 and Ψ_2, respectively (c.f. Eq (4)). The two consecutive band dispersions in **b** are along the path marked by blue dots. The yellow region is a quantum valley Hall (QVH) phase. **d** Evolution of the topological edge states, along the path marked by red dots in (**c**). Color stands for the sublattice polarization $\langle\sigma_z\rangle$. **e** Phase diagram as a function of twisting angle and interlayer bias M, for hybrid moiré excitons with a 25% intralayer component.

environment, which underlies the possibility to tailor η value. In regime of small η, the effect of Förster coupling can be neglected as in earlier discussion of moire excitons in twisted MoTe2[36]. Hereafter, we consider a regime of relatively large η where Förster coupling can qualitatively change the properties of hybrid exciton lattice.

Topological lattice of hybrid moiré excitons

With the p-wave intralayer component, moiré hybrid excitons can have a long radiative lifetime, favorable for the exploration of correlation and topological matters of these composite bosons[41]. Here we show how nontrivial topology can emerge from the Förster VOC in the exciton superlattice, which can be tunable by twisting angle, as well as modest interlayer bias. The latter introduces, through the opposite electric dipoles on the two sublattices, a staggered onsite energy $\varepsilon_i = M$ and $-M$, respectively on B and C sites. The exciton tight-binding Hamiltonian is then,

$$H = \sum_i \varepsilon_i b_i^\dagger b_i - t \sum_{\langle\langle i'i\rangle\rangle} b_{i'}^\dagger \exp\left(i\frac{2\pi}{3}\nu_{i'i}\tau_z\right) b_i + \sum_{\langle i'i\rangle} b_{i'}^\dagger \left[\alpha - \beta(\tau_x \cos 4\varphi_{i'i} + \tau_y \sin 4\varphi_{i'i})\right] b_i \quad (3)$$

The second term is the valley-conserving kinetic propagation in the moiré potential landscape, which is absent between sublattices, and we keep its the leading order effect within each sublattice, i.e., a NNN hopping. Its strength t is an exponential function of moiré period (Fig. 3c)[3]. The momentum space mismatch between the valleys of two layers leads to a constant hopping phase, where $\nu_{i'i} = -\nu_{ii'} = \pm 1$ following the convention shown in Fig. 3c[3] (Supplementary Note 2). The last term is the Förster coupling which we retain only the NN term where $\varphi_{i'i} = 0, \pm\frac{2\pi}{3}$. The $4\varphi_{i'i}$ dependence is then equivalent to $\varphi_{i'i}$, such that intervalley Förster coupling behaves like a Dresselhaus spin–orbit coupling.

At $M = 0$ and $\beta = 0$, this Hamiltonian has two decoupled valley subspaces described by Haldane model of opposite Chern numbers respectively[42], so the system is in a quantum valley Hall phase (QVH), with a topological gap at the mini-Brillouin zone corners $\pm K_M$. It is known that the staggered potential M tends to open a trivial gap at $\pm K_M$[42]. To elucidate the general situation at finite M and β, we track the evolution of the eigenstates at K_M point under these two control parameters (Fig. 4c). Specifically, the first group of states, Ψ_1 and Ψ_2 with eigenenergies $E_{1,2} = -6t \mp M$, are polarized in a single sublattice with valley-sublattice locking. The other two states, Ψ_3 and Ψ_4 with energy $E_{3,4} = 3t \mp \sqrt{9\beta^2 + M^2}$, are spread over both sublattices. The crossover between the two groups defines phase-space boundaries (c.f. Fig. 4b, c):

$$\frac{M}{t} = \pm\left[\frac{9}{2} - \frac{1}{2}\left(\frac{\beta}{t}\right)^2\right]. \quad (4)$$

Inside the area enclosed by the two parabolas, Ψ_3 and Ψ_4 have higher energy than the valley-sublattice polarized states Ψ_1 and Ψ_2, and we find the system in QVH phase with gapless edge states (Fig. 4d, see Supplementary Note 6 for details). Upon the inversion of Ψ_3 with Ψ_1 or Ψ_2 across the boundary defined by Eq. (4), the edge states become gapped.

Lastly, we can map this topological phase diagram to the parameter space spanned by the physical control parameters of twisting angle θ and interlayer bias M. θ determines the moiré period and therefore the NNN kinetic propagation amplitude t (Fig. 3c), as well as the intra- and intervalley Förster coupling strength α and β between the NN (Fig. 2c). The details of their twisting angle dependence are given in Supplementary Note 7). The amplitudes α and β are also controlled by the hybridization weight η and envelope width w of the hybrid moiré exciton. Taking $\eta = 0.25$ and $w = 2$ nm leads to the topological phase diagram shown in Fig. 4e, where the QVH states emerge at twist angle $\theta \geq 2.6°$. We note several simplifications that may quantitatively affect the phase diagram. First of all, the

hybridization weight η can be manipulated by the interlayer bias and the twist angle, and therefore implies its dependence on M and θ. This dependence may quantitatively affect how the phase diagram in the parameter space of M/t and β/t (Fig. 4c) is mapped to the phase diagram in the M and θ parameter space (Fig. 4e), due to the dependence of Förster coupling strength β on M and θ. Secondly, our estimation of the Förster coupling is based on wavepackets trapped at high symmetry MX and XM sites, which can serve as a good basis since Förster coupling is a non-local process not relying on wavefunction overlap. In general, the spread out of the wavefunction shall also depend on the twist angle and moiré potential that is affected by the interlayer bias M, which we did not take into account. On the other hand, as long as the dependence is not drastic, the qualitative feature of the phase diagram shall remain.

Data availability

Data sharing is not applicable to this article, as no datasets were generated or analyzed during the current study.

Received: 25 November 2024; Accepted: 29 April 2025;
Published online: 07 May 2025

References

1. Yu, H., Wang, Y., Tong, Q., Xu, X. & Yao, W. Anomalous light cones and valley optical selection rules of interlayer excitons in twisted heterobilayers. *Phys. Rev. Lett.* **115**, 187002 (2015).
2. Wu, F., Lovorn, T. & MacDonald, A. H. Topological exciton bands in moiré heterojunctions. *Phys. Rev. Lett.* **118**, 147401 (2017).
3. Yu, H., Liu, G.-B., Tang, J., Xu, X. & Yao, W. Moiré excitons: from programmable quantum emitter arrays to spin-orbit-coupled artificial lattices. *Sci. Adv.* **3**, e1701696 (2017).
4. Rivera, P. et al. Interlayer valley excitons in heterobilayers of transition metal dichalcogenides. *Nat. Nanotechnol.* **13**, 1004–1015 (2018).
5. Seyler, K. L. et al. Signatures of moiré-trapped valley excitons in $MoSe_2/WSe_2$ heterobilayers. *Nature* **567**, 66–70 (2019).
6. Tran, K. et al. Evidence for moiré excitons in van der waals heterostructures. *Nature* **567**, 71–75 (2019).
7. Jin, C. et al. Observation of moiré excitons in WSe_2/WS_2 heterostructure superlattices. *Nature* **567**, 76–80 (2019).
8. Alexeev, E. M. et al. Resonantly hybridized excitons in moiré superlattices in van der Waals heterostructures. *Nature* **567**, 81–86 (2019).
9. Huang, D., Choi, J., Shih, C.-K. & Li, X. Excitons in semiconductor moiré superlattices. *Nat. Nanotechnol.* **17**, 227–238 (2022).
10. Rivera, P. et al. Valley-polarized exciton dynamics in a 2D semiconductor heterostructure. *Science* **351**, 688–691 (2016).
11. Zhang, C. et al. Interlayer couplings, moiré patterns, and 2D electronic superlattices in MoS_2/WSe_2 hetero-bilayers. *Sci. Adv.* **3**, e1601459 (2017).
12. Brotons-Gisbert, M. et al. Spin–layer locking of interlayer excitons trapped in moiré potentials. *Nat. Mater.* **19**, 630–636 (2020).
13. Baek, H. et al. Highly energy-tunable quantum light from moiré-trapped excitons. *Sci. Adv.* **6**, eaba8526 (2020).
14. Yu, H., Liu, G.-B. & Yao, W. Brightened spin-triplet interlayer excitons and optical selection rules in van der Waals heterobilayers. *2D Mater.* **5**, 035021 (2018).
15. Jin, C. et al. Identification of spin, valley and moiré quasi-angular momentum of interlayer excitons. *Nat. Phys.* **15**, 1140–1144 (2019).
16. Li, W., Lu, X., Dubey, S., Devenica, L. & Srivastava, A. Dipolar interactions between localized interlayer excitons in van der Waals heterostructures. *Nat. Mater.* **19**, 624–629 (2020).
17. Xiong, R. et al. Correlated insulator of excitons in WSe_2/WS_2 moiré superlattices. *Science* **380**, 860–864 (2023).
18. Park, H. et al. Dipole ladders with large Hubbard interaction in a moiré exciton lattice. *Nat. Phys.* **19**, 1286–1292 (2023).
19. Hsu, W.-T. et al. Tailoring excitonic states of van der Waals bilayers through stacking configuration, band alignment, and valley spin. *Sci. Adv.* **5**, eaax7407 (2019).
20. Zhang, L. et al. Twist-angle dependence of moiré excitons in $WS_2/MoSe_2$ heterobilayers. *Nat. Commun.* **11**, 5888 (2020).
21. Zhao, S. et al. Hybrid moiré excitons and trions in twisted $MoTe_2$–$MoSe_2$ heterobilayers. *Nano Lett.* **24**, 4917–4923 (2024).
22. Yu, H., Liu, G.-B., Gong, P., Xu, X. & Yao, W. Dirac cones and Dirac saddle points of bright excitons in monolayer transition metal dichalcogenides. *Nat. Commun.* **5**, 3876 (2014).
23. Qiu, D. Y., Cao, T. & Louie, S. G. Nonanalyticity, valley quantum phases, and lightlike exciton dispersion in monolayer transition metal dichalcogenides: Theory and first-principles calculations. *Phys. Rev. Lett.* **115**, 176801 (2015).
24. Liu, L. Y. et al. Direct observation of massless excitons and linear exciton dispersion. Preprint at *arXiv* https://doi.org/10.48550/arXiv.2502.20454 (2025).
25. Selig, M., Malic, E., Ahn, K. J., Koch, N. & Knorr, A. Theory of optically induced Förster coupling in van der Waals coupled heterostructures. *Phys. Rev. B* **99**, 035420 (2019).
26. Baimuratov, A. S. & Högele, A. Valley-selective energy transfer between quantum dots in atomically thin semiconductors. *Sci. Rep.* **10**, 16971 (2020).
27. Hichri, A., Amand, T. & Jaziri, S. Resonance energy transfer from moiré-trapped excitons in $MoSe_2/WSe_2$ heterobilayers to graphene: Dielectric environment effect. *Phys. Rev. Mater.* **5**, 114002 (2021).
28. Li, C. & Yao, W. Cross-dimensional valley excitons from Förster coupling in arbitrarily twisted stacks of monolayer semiconductors. *2D Mater.* **11**, 015006 (2023).
29. Clegg, R. M. *The History of Fret*. 1–45 https://doi.org/10.1007/0-387-33016-X_1 (Springer US, Boston, MA, 2006).
30. Cai, J. et al. Signatures of fractional quantum anomalous Hall states in twisted $MoTe_2$. *Nature* **622**, 63–68 (2023).
31. Park, H. et al. Observation of fractionally quantized anomalous Hall effect. *Nature* **622**, 74–79 (2023).
32. Zeng, Y. et al. Thermodynamic evidence of fractional Chern insulator in moiré $MoTe_2$. *Nature* **622**, 69–73 (2023).
33. Xu, F. et al. Observation of integer and fractional quantum anomalous Hall effects in twisted bilayer $MoTe_2$. *Phys. Rev. X* **13**, 031037 (2023).
34. Weston, A. et al. Interfacial ferroelectricity in marginally twisted 2D semiconductors. *Nat. Nanotechnol.* **17**, 390–395 (2022).
35. Wang, X. et al. Interfacial ferroelectricity in rhombohedral-stacked bilayer transition metal dichalcogenides. *Nat. Nanotechnol.* **17**, 367–371 (2022).
36. Yu, H. & Yao, W. Luminescence anomaly of dipolar valley excitons in homobilayer semiconductor moiré superlattices. *Phys. Rev. X* **11**, 021042 (2021).
37. Tong, Q. et al. Topological mosaics in moiré superlattices of van der Waals heterobilayers. *Nat. Phys.* **13**, 356–362 (2017).
38. Bistritzer, R. & MacDonald, A. H. Moiré bands in twisted double-layer graphene. *Proc. Natl Acad. Sci. USA* **108**, 12233–12237 (2011).
39. Wang, Y., Wang, Z., Yao, W., Liu, G.-B. & Yu, H. Interlayer coupling in commensurate and incommensurate bilayer structures of transition-metal dichalcogenides. *Phys. Rev. B* **95**, 115429 (2017).
40. Baer, R. & Rabani, E. Theory of resonance energy transfer involving nanocrystals: the role of high multipoles. *J. Chem. Phys.* **128**, 184710 (2008).
41. Xie, M., Hafezi, M. & Das Sarma, S. Long-lived topological flatband excitons in semiconductor moiré heterostructures: a bosonic Kane-Mele model platform. *Phys. Rev. Lett.* **133**, 136403 (2024).
42. Haldane, F. D. M. Model for a quantum hall effect without Landau levels: condensed-matter realization of the "parity anomaly". *Phys. Rev. Lett.* **61**, 2015–2018 (1988).

Acknowledgements
This work is supported by the National Key R&D Program of China (2020YFA0309600), the Research Grant Council of Hong Kong (AoE/P-701/20, HKU SRFS2122-7S05, A-HKU705/21), and New Cornerstone Science Foundation.

Author contributions
W.Y. conceived and supervised the research. H.Z. performed the calculations with important inputs from C.L., and H.Y. All authors analyzed and discussed the results. H.Z. and W.Y. wrote the paper.

Competing interests
The authors declare no competing interests.

Additional information
Supplementary information The online version contains supplementary material available at https://doi.org/10.1038/s42005-025-02114-0.

Correspondence and requests for materials should be addressed to Wang Yao.

Peer review information *Communications Physics* thanks the anonymous reviewers for their contribution to the peer review of this work.